International Journal of Hydrogen Energy 177 (2025) 151577

Contents lists available at ScienceDirect

International Journal of Hydrogen Energy

journal homepage: www.elsevier.com/locate/he

A new family of compositionally complex perovskite oxides $Sr(Ti_{(1-x)/3}Mn_{(1-x)/3}Fe_{(1-x)/3}Cr_x)O_3$ for solar thermochemical hydrogen production

Ha Ngoc Ngan Tran [a,1], Cijie Liu [b,1], Dawei Zhang [c,1], Qingyuan Li [b], Jingjing Yang [c], Shaoshuai Chen [b], Wei Li [b,*], Li Li [d], Qingsong Wang [d], Héctor A. De Santiago [b], Liang Ma [b], Yi Wang [b], Gregory Collins [b], Jian Luo [c,e,**], Xingbo Liu [b,***]

[a] Department of Chemical and Biomedical Engineering, Benjamin M. Statler College of Engineering and Mineral Resources, West Virginia University, Morgantown, WV, 26506, USA
[b] Department of Mechanical, Materials and Aerospace Engineering, Benjamin M. Statler College of Engineering and Mineral Resources, West Virginia University, Morgantown, WV, 26506, USA
[c] Program in Materials Science and Engineering, University of California San Diego, La Jolla, CA, 92093, USA
[d] Bavarian Center for Battery Technology (BayBatt), Department of Chemistry, University of Bayreuth, Universitätsstr. 30, 95447, Bayreuth, Germany
[e] Aiiso Yufeng Li Family Department of Chemical and Nano Engineering, University of California San Diego, La Jolla, CA, 92093, USA

ARTICLE INFO

Handling Editor: Umit Demirci

Keywords:
Solar thermochemical hydrogen
Perovskite oxides
High entropy oxides
Chemical looping
Oxygen non-stoichiometry

ABSTRACT

Solar thermochemical hydrogen (STCH) production using non-stoichiometric redox oxides for two-step water-splitting in a chemical looping way is a promising technology for sustainable solar H_2 production. Perovskite oxides have attracted significant interest due to their favorable thermodynamic properties. However, their H_2 production, cycling and phase stability, and scalability are still limited due to a limited compositional space in traditional perovskite oxides. Specifically, costly rare earth and critical transition metal elements are generally used, restricting their economic viability for large-scale applications. Expanding from the emerging field of high-entropy ceramics, this work explores a new family of compositionally complex perovskite oxides (CCPOs), $Sr(Ti_{(1-x)/3}Mn_{(1-x)/3}Fe_{(1-x)/3}Cr_x)O_3$, with tunable Cr content (x) from 0 to 0.25 for STCH production. Notably, this class of CCPOs eliminates the use of expensive rare earth and critical transition metals for STCH applications. This study shows that increasing the Cr content to 0.2 enhances the hydrogen production of $Sr(Ti_{0.2667}Mn_{0.2667}Fe_{0.2667}Cr_{0.2})O_3$ to 380 μmol/g in a short 1-h two-step redox duration, surpassing $Sr(Ti_{0.333}Mn_{0.333}Fe_{0.333})O_3$ with a hydrogen production of 228 μmol/g. Additionally, entropy stabilization may contribute to the phase stability during thermochemical redox cycling, enabling a relatively stable H_2 production of $Sr(Ti_{0.2667}Mn_{0.2667}Fe_{0.2667}Cr_{0.2})O_3$ over 21 cycles. This study provides a new class of CCPOs composed of relatively low-cost alkaline earth and transition metals with great potential for STCH and other chemical looping applications.

1. Introduction

The conversion of intermittent solar radiation into storable and transportable chemical fuels provides a pathway to sustainable feedstocks and dispatchable power sources [1,2]. Hydrogen is a clean and sustainable energy carrier that can store the intermittent solar energy. The promising solar-driven water splitting technologies for H_2 production include photocatalytic and photoelectrochemical water splitting, photovoltaic-driven water electrolysis, and solar thermochemical water splitting [3–6]. The photocatalytic, photoelectrochemical and photovoltaic-driven approaches employ the sunlight with a narrow range of solar spectrum, while the solar thermochemical water splitting driven by the concentrated solar power can utilize the full solar spectrum energy. The direct water thermolysis suffers from low water dissociation even at extremely high temperatures (>2000 K) and challenges of separation of H_2 and O_2 [7]. Therefore, the two-step solar

* Corresponding author.
** Corresponding author. Program in Materials Science and Engineering, University of California San Diego, La Jolla, CA, 92093, USA.
*** Corresponding author.
E-mail addresses: liweicsiro@gmail.com (W. Li), jluo@alum.mit.edu (J. Luo), xingbo.liu@mail.wvu.edu (X. Liu).
[1] These authors (H.N.N.T., C.L., and D.Z.) contributed equally to this work.

https://doi.org/10.1016/j.ijhydene.2025.151577
Received 6 April 2025; Received in revised form 4 September 2025; Accepted 15 September 2025
Available online 20 September 2025

thermochemical hydrogen (STCH) production has attracted considerable attention as it can effectively utilize the full solar spectrum energy, lower the temperature, and separate the H_2 and O_2 products in a chemical looping way [8].

Typically, the two-step STCH process involves a high-temperature endothermic reduction step (≥1200 °C) under low oxygen partial pressure (P_{O_2}) with a suitable non-stoichiometric metal oxide to produce oxygen (Eq. (1)), and a subsequent exothermic oxidation step through flowing steam to the reduced metal oxide for water splitting (Eq. (2)) at a relatively lower temperature (800−1100 °C) as follows,

$$\frac{1}{\delta}MO_x \rightarrow \frac{1}{\delta}MO_{x-\delta} + \frac{1}{2}O_2 \quad \text{(Eq. 1)}$$

$$\frac{1}{\delta}MO_{x-\delta} + H_2O \rightarrow \frac{1}{\delta}MO_x + H_2 \quad \text{(Eq. 2)}$$

where δ is the off-stoichiometry indicating the extent of reduction [6,9]. The metal oxide serves the redox center to enable the chemical looping. Note that the metal-oxide reduction reaction enthalpy must be higher than the water-splitting reaction enthalpy at the reoxidation temperature and tends to range between 250 and 500 kJ/mol of H_2 [10]. Temperature, partial pressure of oxygen, and concentration of gases play key roles in these reactions. The reduction reaction depends sensitively on temperature and P_{O_2}. The reoxidation reaction highly depends on both temperature and the amount of excess reactant steam relative to available oxygen ion vacancies. From the thermodynamic perspective, the lower reoxidation temperature enables higher H_2 production. However, a lower reoxidation temperature requires extracting a large amount of sensible heat after the reduction step and then injecting a similar amount to raise the temperature of the material in preparation for the next reduction step. In addition, the kinetics of thermal reduction and oxidation of metal oxide depend on temperature, partial pressure of oxygen, and concentration of gases.

Ceria ($CeO_{2-\delta}$) has been widely investigated as a family of non-stoichiometric metal oxides for STCH due to its phase stability and fast redox kinetics [11–15]. However, ceria requires extremely high reduction temperature (>1500 °C) to achieve a small extent of reduction (Δδ ≈ 0.03–0.06), posing challenges for STCH reactor designs and industrially viable H_2 production [16–20]. In contrast, the perovskite oxides ($ABO_{3-\delta}$) are regarded as a class of promising redox oxide alternative candidates to ceria for STCH, as they can reach large non-stoichiometry redox swing at lower temperatures, and have relatively high stability, tunable defect chemistry with A/B site doping, and a large compositional space [21–26]. For example, several perovskite oxides such as $Sr_xLa_{1-x}Mn_yAl_{1-y}O_{3-\delta}$ (SLMA), $La_{0.6}Ca_{0.4}Mn_{1-y}Al_yO_{3-\delta}$ (LCMA), and $Ca(Ti_{0.5}Mn_{0.5})O_3$ have been investigated for STCH [16,27,28]. To further enhance the redox kinetics or phase stability, high-entropy oxides (HEOs) have recently developed for STCH [29–32]. Later, compositionally complex ceramics have been introduced to broaden the field of high entropy ceramics by exploring non-equimolar compositions, as well as long- and short-range orders, which reduce the configurational entropy but allow more engineering space to tailor and improve the properties [33,34]. Specifically, compositionally complex perovskite oxides (CCPOs) such as $(La_{1-y}Sr_y)(Mn_{(1-x)/3}Fe_{(1-x)/3}Co_xAl_{(1-x)/3})O_3$, $(La_{1-x}Sr_x)(Mn_{1/3}Fe_{1/3}Ti_{1/3})O_{3-\delta}$, and $(La_{1-x}Sr_x)(Mn_{1/3}Fe_{1/3}Cr_{1/3})O_{3-\delta}$ have emerged as promising redox perovskite oxides for STCH [35–37]. Although these CCPOs feature non-equimolar compositions and often lower configurational entropy compared to HEOs with equimolar elemental compositions, they create new opportunities to tune unique local ordering, distortion, and redox activities and balance thermodynamic and kinetic properties. The progress of perovskite oxides developments for STCH has been reviewed [8]. Most of the reported perovskite oxide compositions contain rare earth metals (e.g. La, Ce, and Y) and costly critical transition metals (e.g. Co), limiting their economic viability for scalable STCH applications. It is highly desired to develop redox-active and stable CCPOs with low-cost alkaline earth and transition metal elements.

Herein, a new class of CCPOs is reported for two-step STCH with chemical formula $Sr(Ti_{(1-x)/3}Mn_{(1-x)/3}Fe_{(1-x)/3}Cr_x)O_3$, denoted as STMFCx for brevity, which are composed of low-cost earth-abundant alkaline earth and transition metal elements. This STMFCx series of CCPOs show high phase stability during the STCH redox. Cr seems to be the major redox active element among B-site elements influencing the extent of reduction. STMFC0.2 demonstrates a high STCH production of 380 μmol/g within a short 1-h redox duration under optimal STCH conditions and excellent stability for 21 cycles. This work paves the way for the rational design of cost-effective rare earth and critical metal-free CCPOs for the STCH application. The concept of CCPO design may guide the future development of metal oxides for thermochemical looping and catalysis [38].

2. Experimental Procedure

2.1. Materials synthesis

STMFCx series powders were prepared using a solid-state method as previously reported [35,37]. The starting chemical precursors including $SrCO_3$ (Alfa Aesar, 99.99 %), TiO_2 (Alfa Aesar, 99.9 %), Cr_2O_3 (Alfa Aesar, 99 %), MnO_2 (Alfa Aesar, 99.9 %), and Fe_2O_3 (Alfa, Aesar, 99.5 %) were used without further purification. These powders were mixed based on a calculated stoichiometric ratio in a poly (methyl methacrylate) high-energy ball mill (HEBM) vial with 2 wt% steric acid. Tungsten carbide endcaps and milling balls were used, and the mixture was dry milled for 100 min using a SPEX 8000D high-energy ball mill (SPEX SamplePrep, USA). The mixed powder was then heated at a rate of 5 °C/min and annealed in air at 1300 °C for 10 h. After cooling, the product powder was ground by a pestle and mortar and then further heated at the same ramping rate and annealed in air at 1400 °C for 10 h to improve the homogeneity and purity of final products.

2.2. Materials characterization

The phases of synthesized materials were characterized using X-ray diffraction (XRD) on an X'Pert Pro X-ray diffractometer (PANalytical), operating at 45 kV and 40 mA with Cu Kα radiation. The Rietveld Refinement was conducted using GSAS-II software to analyze the crystal structures and determine specific crystallographic parameters. The crystallographic information file (CIF) of $SrMn_{0.5}Ti_{0.5}O_3$ (space group $Pm\bar{3}m$) from the Inorganic Crystal Structure Database (ICSD #18–5588) served as a starting structure model.

The elemental composition and stoichiometry of the samples were determined through the inductively coupled plasma mass spectrometry (ICP-MS) method, using the PerkinElmer NexION 2000 ICP Mass Spectrometer for digested solutions following the EPA 200.8 method.

The microstructure and elemental homogeneity of the materials were examined with a scanning electron microscopy (SEM, FEI Apreo), equipped with energy-dispersive X-ray (EDX, Oxford N-MAX) spectroscopy. The high-angle annular dark field scanning transmission electron microscopy (HAADF-STEM) with EDX was performed using ThermoFisher Talos 200X operating at 200 kV. Raman spectra were acquired by the RENISHAW INVIA Raman spectrometer with a laser excitation wavelength of 532 nm. XPS measurements were carried out using a PHI VersaProbe 5000 Scanning X-ray Photoelectron Spectrometer (ULVAC-PHI, Inc.) at room temperature under ultra-high vacuum conditions (<1×10^{-6} Pa). A monochromatic Al Kα X-ray source (photon energy: 1486 eV, power: 25 W) with a 100 μm spot size was used for excitation. All binding energies were calibrated against the C 1s peak at 284.8 eV.

Synchrotron X-ray absorption spectroscopy (XAS) measurements at Cr K-edge, Fe K-edge, and Mn K-edge were performed at beamline KMC2 of BESSY II light source (Berlin, Germany). XAS spectra were recorded in transmission mode. STMFC0.1 was reduced in N_2 at 1350 °C for 2 h and

then sent for *ex situ* XAS characterization.

2.3. Temperature-programmed reduction (TPR) experiment

Temperature-programmed reduction (TPR) experiments were performed using a simultaneous thermal gravimetric analyzer (NETZSCH STA 449 F3 Jupiter). Approximately 30 mg of each sample was loaded into an alumina crucible with a Pt foil as an interlayer for analysis. The samples were heated to 1350 °C at a ramping rate of 30 °C/min and held isothermally for 45 min under ultrahigh-purity (UHP) Ar. Then, the samples were cooled down to 1100 °C at the same rate under Ar. Subsequently, the mixture gas of 21 % O_2 and 79 % Ar was introduced to re-oxidize the samples. A blank crucible was used to calibrate the mass loss curves. The extent of reduction (Δδ) was determined by measuring the mass change using the formula:

$$\Delta\delta = \frac{\Delta m \cdot M_s}{m_s \cdot M_O} \quad \text{(Eq. 3)}$$

where Δm is the mass loss, M_s is the molar mass of the sample, m_s is the initial sample mass, and M_O is the molar mass of oxygen.

The first cycle commonly exhibited activation behaviors due to the surface oxidation and adsorption. Therefore, the stabilized cycles were used for comparison across all samples.

2.4. Thermochemical water splitting

The STCH performance of the materials was evaluated using a homemade flow reactor, integrating the steam generator, heating and gas analysis units, to simulate the high-temperature conditions of real-world solar thermochemical hydrogen reactor systems in a controlled laboratory setting (Fig. S1). A packed bed reactor integrated with programmable high-temperature electric furnace (Carbolite HTF 17/5) was employed. Approximately 100 mg of powder was loaded into the center of a 24-inch alumina tube (AdValue Technology, OD: 1/4″, ID: 3/16″) placed horizontally near a thermocouple within the electric furnace. The powder was evenly distributed inside the tube center close to the thermocouple to ensure adequate gas–solid contact and mass transfer, with a void above the powder to prevent sudden pressure drop and particle loss. Nitrogen (UHP, Matheson) was used as a carrier gas, and the flow rate was precisely regulated using a calibrated mass flow controller (Alicat Scientific). Note that although an electric furnace was used instead of a concentrated solar power reactor, STCH was still used to describe the thermochemical water splitting process and performance following the community practice.

Steam, at a concentration of 40 vol% H_2O, was generated using a water evaporator (Fuel Cell Technologies, Inc.) heated to 85 °C and mixed with nitrogen via a series of flow redirection valves. The reactor outlet was connected to a cold trap to condense and remove excess steam. To eliminate the possible errors of integrating the mass spectrometry response, the total H_2 production during each cycle was collected with a gas sampling bag (Restek Multilayer Foil) for a given time. The H_2 concentration in the collected gas bag was quantified using the gas chromatography (Shimadzu GC-2014) with a thermal conductivity detector (TCD), which was calibrated with a series of standard H_2 gases. Calibration was performed using certified H_2 gas standards (GASCO, Cal Gas Direct Inc.) with known concentrations balanced by N_2. The effects of the reduction temperature, oxidation temperature, and flow rate on H_2 production were investigated. The oxidation temperature was fixed at 1100 °C, while the reduction temperatures were controlled at 1100, 1150, 1250, 1350, and 1400 °C. The reduction temperature was fixed at 1350 °C, while the oxidation temperatures were controlled at 800, 900, 1000, and 1100 °C. The total duration of each cycle was controlled to be 1 h. STCH tests were conducted across a range of reduction/oxidation durations. The gas flow rates were controlled at 100, 200, or 300 sccm. Background H_2 production from catalytic water thermolysis at different temperatures was subtracted from the total H_2 production, and only the H_2 production from the thermochemical redox reaction was presented.

3. Results and discussion

3.1. Materials characterization

The nominal composition of the prepared samples can be described by the general formula of $Sr(Ti_{(1-x)/3}Mn_{(1-x)/3}Fe_{(1-x)/3}Cr_x)O_3$. In this work, $Sr(Ti_{(1-x)/3}Mn_{(1-x)/3}Fe_{(1-x)/3}Cr_x)O_3$ materials were synthesized by the solid-state synthesis based on the mixture of starting metal oxides and carbonate at a stoichiometric ratio with the adjusted content of Cr ranging from 0 to 0.25. Table 1 summarizes the sample nominal compositions and abbreviations.

XRD patterns reveal that the materials exhibit archetypical cubic perovskite crystal structures (with space group $Pm\bar{3}m$) (Fig. 1a). This structure represents a typical high-symmetry perovskite, with Sr occupies the typical large 12-coordinate cuboctahedra site, and mixed occupancy of Ti, Mn, Fe and Cr on the B-site providing potential flexibility in tailoring its properties (Fig. 1b). The XRD diffraction peaks shift toward the lower diffraction angle direction with the increase of Cr content (Fig. 1c), suggesting the lattice expansion due to the larger Cr ionic size. Fig. 1d displays the Raman spectra of STMFCx. In the cubic perovskite structure (space group $Pm\bar{3}m$), where every atom in the structure is at an inversion center, Raman scattering is symmetry-forbidden [39–41]. The distortions (tilting, octahedral distortion, and A-cation displacement) can break the cubic symmetry. Thus, the bands in the cubic phase are usually observed to arise from second-order scattering, which results from the combinations of phonons at different points in the Brillouin zone. In STMFCx, broad peaks are in the ranges of 200–800 cm^{-1}, which can be attributed to the second-order scattering. The effects of B-site cation substitution in ABO_3 perovskites are found. The low-frequency mode around 290 cm^{-1} is assigned to Ag symmetry based on the extension of single-crystal literature data, which can be linked to the displacement of Mn ions in this situation [39,42,43]. On the other hand, a broad band around 525 cm^{-1} is also observed with Ag symmetry. This peak around 500 cm^{-1} is likely the result of two overlapping bands, which can be considered as a result of the first – order scattering due to the activation of the bulk Ti–O stretching phonon mode and local modes, such as the Jahn-Teller-active antisymmetric stretching vibrational mode of MnO_6 octahedral, which is attributed to Mn atoms occupying B-site [43–45]. Notably, the peak at 680 cm^{-1} in STMFC0 shifted as the Cr concentration increases. This peak appears in Mn-substituted perovskite oxide samples, and its intensity increases with the concentration of substituents, with the most pronounced increase occurring with Cr doping due to their multiple valence states that may induce Jahn – Teller distortion [46–48]. In this case, this effect is explained with an increase in the tolerance factor with increased Cr content, which enhances the structural disorder [49]. As the Cr content increases, lattice distortion enhances the charge transfer interactions between Fe and Cr ions, strengthening electron – phonon coupling and intensifying this peak. In STMFC0.2 sample, the vibrational band is close to 700 cm^{-1} exhibiting Ag symmetry, which corresponds to an in–phase

Table 1
Compositions and sample abbreviations of synthesized $Sr(Ti_{(1-x)/3}Mn_{(1-x)/3}Fe_{(1-x)/3}Cr_x)O_3$.

Nominal composition	Sample Abbreviation
$Sr(Ti_{0.333}Mn_{0.333}Fe_{0.333})O_3$	STMFC0
$Sr(Ti_{0.3167}Mn_{0.3167}Fe_{0.3167}Cr_{0.05})O_3$	STMFC0.05
$Sr(Ti_{0.3}Mn_{0.3}Fe_{0.3}Cr_{0.1})O_3$	STMFC0.1
$Sr(Ti_{0.2833}Mn_{0.2833}Fe_{0.2833}Cr_{0.15})O_3$	STMFC0.15
$Sr(Ti_{0.2667}Mn_{0.2667}Fe_{0.2667}Cr_{0.2})O_3$	STMFC0.2
$Sr(Ti_{0.25}Mn_{0.25}Fe_{0.25}Cr_{0.25})O_3$	STMFC0.25

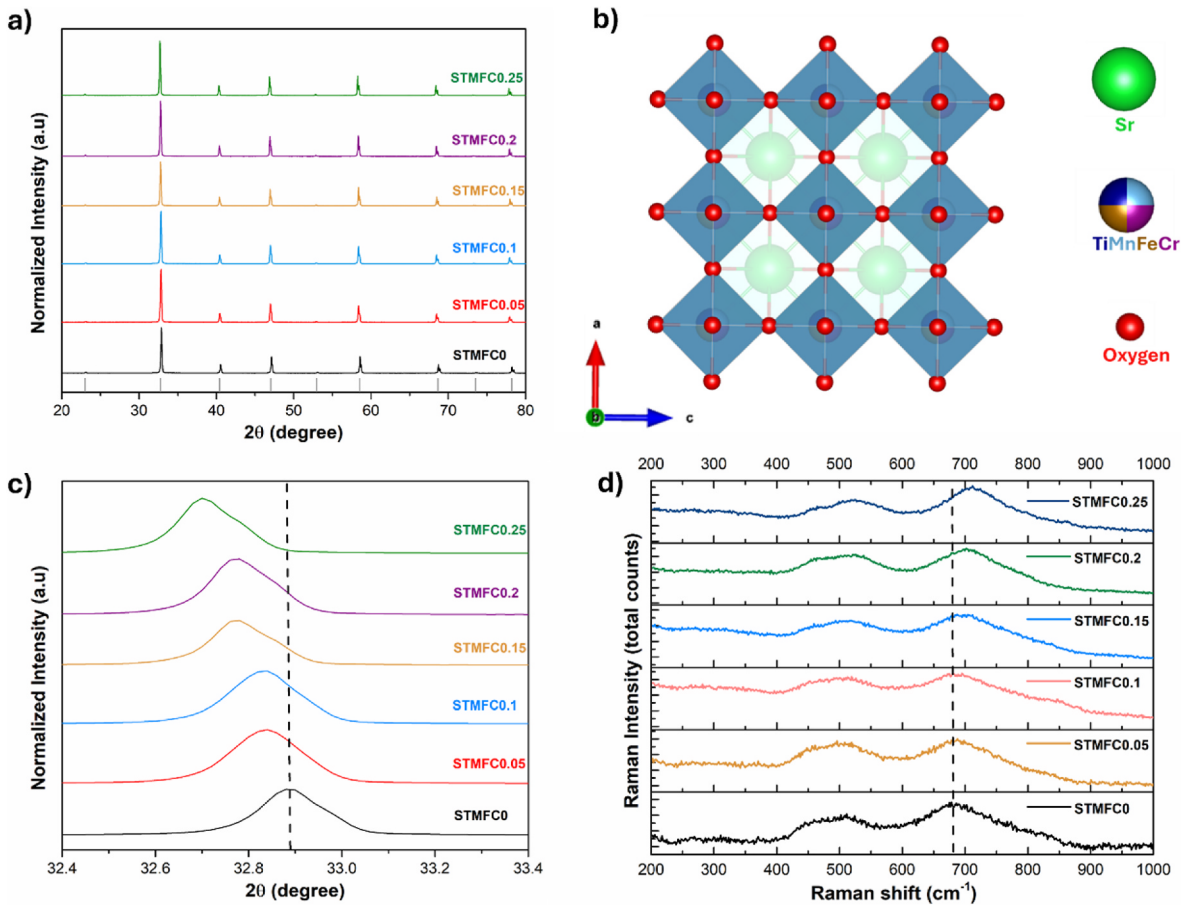

Fig. 1. a) XRD patterns of STMFCx series with a standard XRD PDF card for $SrTi_{0.5}Mn_{0.5}O_3$ (PDF#18–5588) as a reference. b) Crystal structure of STMFC perovskite oxide. c) Enlarged area of main 011 peak in the XRD patterns showing peak shifting. d) Raman spectra of STMFCx.

oxygen stretching mode in the vicinity of the substituted Cr ion around Fe cation [50,51]. This peak becomes more pronounced when there are both Fe and Cr ions present in the B-site, which is activated by charge transfer between Fe and Cr ions attributed to orbital-mediated electron-phonon coupling. This configuration is considered to be Jahn-Teller active, which causes a volume-preserving lattice distortion characterized by stretching of Fe(Cr) – O bonds along the z-axis and compression in the x-y plane [49,52].

Rietveld refinement further confirms the $Pm\bar{3}m$ space group (Fig. 2) with an increase in these lattice distances, consistent with the shift in the diffraction peak positions. The refined crystallographic structures agree well with the observed diffraction patterns as indicated by the final goodness-of-fit (R_w) of less than 6 % for all refinements (Table 2). Furthermore, the ICP-MS analysis confirms that the real bulk compositions of the synthesized powders are consistent with their nominal compositions (Table 3). The morphologies, microstructure, and elemental distribution of STMFC0.2 were characterized using SEM in combination with the EDX spectroscopy (Fig. 3). STMFC0.2 shows irregular micrometer-sized particles with partial agglomeration. The unit particles have an average diameter of 2.03 ± 0.13 μm (Fig. S2a and b). The atomic ratio from EDX is close to that from ICP-MS.

3.2. Temperature-programmed reduction analysis

The thermochemical redox capability of STMFCx samples were measured by the TPR method. Fig. 4a shows their TPR curves. The reversible extent of reduction (Δδ) reflects the degree of non-stoichiometry arising from the formation of oxygen vacancies under a high temperature with lower oxygen partial pressure and the reversibility under higher oxygen partial pressure. Δδ apparently increases with the Cr content from 0 to 0.1 and then shows slight growth with further increase of Cr content. When $x \leq 0.2$, the reduced STMFCx samples are been fully re-oxidized. In contrast, STMFC0.25 shows a minor irreversibility of δ, which is generally due to the potential irreversible phase transformation or secondary phase segregation during redox cycling [53].

3.3. Analysis of the possible redox metal

The oxidation state, local coordination, and electronic structure of Cr, Fe and Mn atoms in STMFC0.1 were examined using ex situ X-ray Absorption Near Edge Spectroscopy (XANES), identifying the valence changes of Cr, Fe and Mn elements in the bulk after the thermal reduction. Fig. 4b presents the normalized Cr K-edge XANES spectra of pristine and reduced STMFC0.1 samples. The Cr K-edge transition, associated with the dipole excitation of electrons from the Cr 1s orbital to unoccupied 3d orbitals, shifts to lower energy in the post-reduction sample [54,55]. This signifies a reduction in Cr oxidation state, which is linked to the oxygen vacancy formation during the high-temperature reduction reaction. The energy of Fe K-edge absorption edge of the reduced sample is slightly changed compared to that of pristine sample (Fig. 4c). In addition, the white line intensity decreases in the reduced sample, which suggests the filling of *d*-electrons and reduction of Fe element and minor electronic changes. This indicates that Fe may show a minor reduced oxidation state after thermal reduction. In contrast, the Mn K-edge XANES spectra of pristine and reduced STMFC0.1 (Fig. 4d) show negligible edge and white line position shifts, indicating that Mn likely remains unchanged during the thermal reduction. Note that the

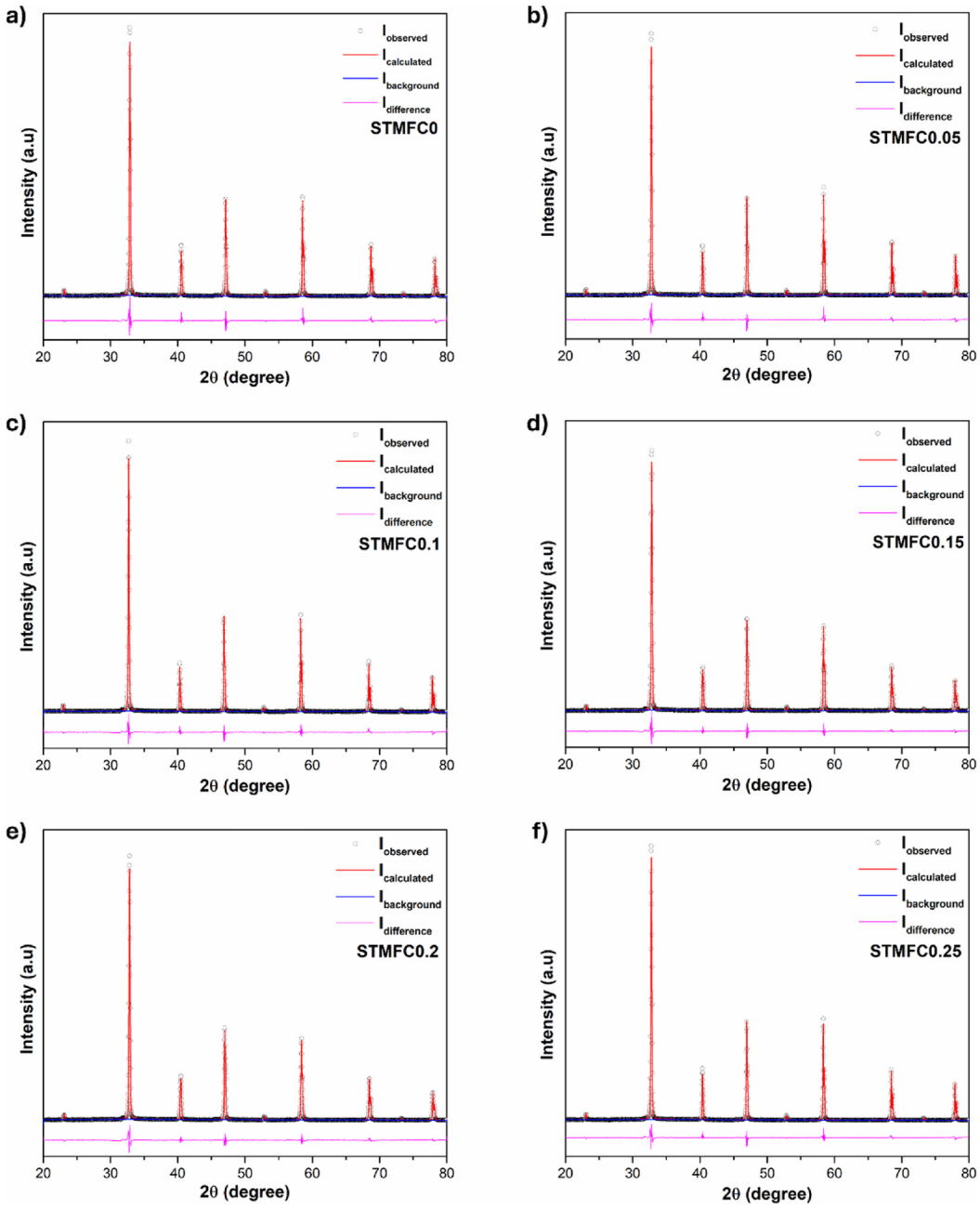

Fig. 2. Rietveld refinements of XRD patterns of synthesized STMFCx samples with the *Pm*$\bar{3}$m cubic phase structure.

Table 2
Structural refinement parameters obtained by Rietveld refinements of XRD patterns of STMFCx.

Sample	Lattice Parameter a (Å)	R_w (%)
STMFC0	3.86456	5.38
STMFC0.05	3.87482	5.59
STMFC0.1	3.87901	5.58
STMFC0.15	3.87947	5.23
STMFC0.2	3.88053	5.51
STMFC0.25	3.88062	5.39

Table 3
ICP-MS results of the metal ion atomic ratio for STMFCx.

Nominal composition	Real composition measured by ICP-MS
$Sr(Ti_{0.333}Mn_{0.333}Fe_{0.333})O_3$	$Sr(Ti_{0.3251}Mn_{0.3356}Fe_{0.3393})O_3$
$Sr(Ti_{0.3167}Mn_{0.3167}Fe_{0.3167}Cr_{0.05})O_3$	$Sr(Ti_{0.3057}Mn_{0.3192}Fe_{0.3249}Cr_{0.0502})O_3$
$Sr(Ti_{0.3}Mn_{0.3}Fe_{0.3}Cr_{0.1})O_3$	$Sr(Ti_{0.3126}Mn_{0.2677}Fe_{0.3171}Cr_{0.1026})O_3$
$Sr(Ti_{0.2833}Mn_{0.2833}Fe_{0.2833}Cr_{0.15})O_3$	$Sr(Ti_{0.2745}Mn_{0.2910}Fe_{0.2831}Cr_{0.1514})O_3$
$Sr(Ti_{0.2667}Mn_{0.2667}Fe_{0.2667}Cr_{0.2})O_3$	$Sr(Ti_{0.2591}Mn_{0.2714}Fe_{0.2683}Cr_{0.2012})O_3$
$Sr(Ti_{0.25}Mn_{0.25}Fe_{0.25}Cr_{0.25})O_3$	$Sr(Ti_{0.2451}Mn_{0.2531}Fe_{0.2516}Cr_{0.2502})O_3$

reduced sample was inevitably exposed to air when transferred from the furnace to the synchrotron XAS beam, which may partially oxidize the metal centers. Based on the present findings, it is proposed that Cr may be the major redox active metal, while Fe may show minor redox change during the high-temperature reduction. Mn might play a coordination role in stabilizing the structure.

The XPS spectra (Fig. S3) of pristine STMFC0, STMFC0.1, and STMFC0.2 were investigated. The XPS survey of STMFC0.2 (Fig. S3a) confirms the elemental composition. The Sr 3d peaks of STMFCx

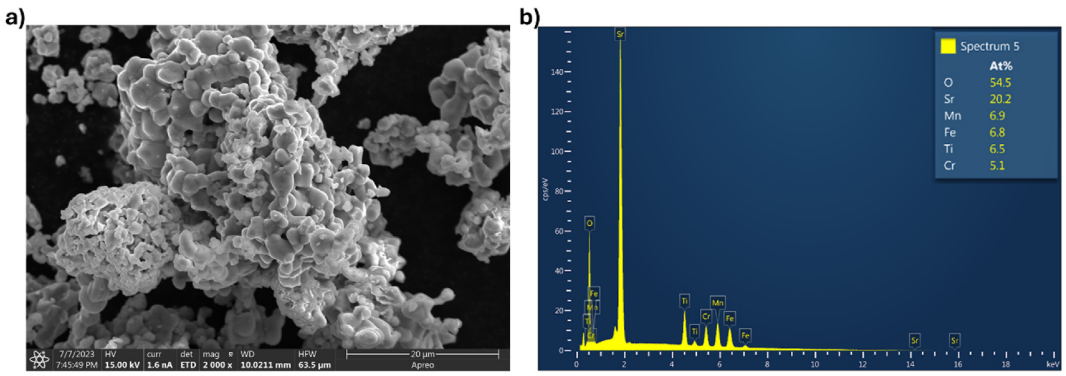

Fig. 3. a) SEM images and b) corresponding EDX result showing the content of Sr, Ti, Mn, Fe, and Cr in pristine STMFC0.2.

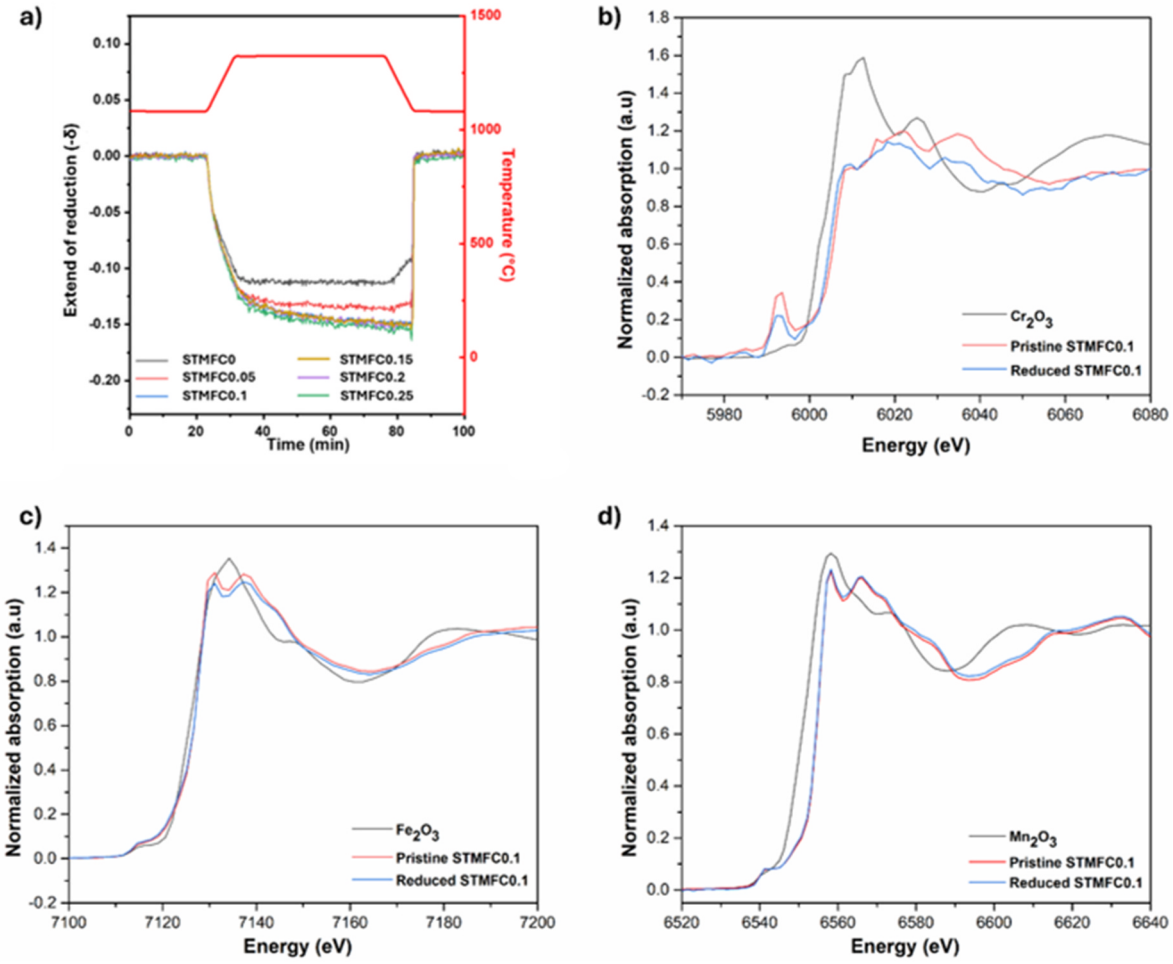

Fig. 4. a) TPR curves showing the reversibility and the extent of reduction (Δδ) for STMFCx with x ranging from 0 to 0.25 during reduction in Ar at 1350 °C followed by oxidation in 21 % O_2 balanced by Ar at 1100 °C. b) Normalized Cr K-edge XANES spectra of pristine STMFC0.1 and reduced counterpart as well as reference Cr_2O_3 standard. c) Normalized Fe K-edge XANES spectra of pristine STMFC0.1 and reduced counterpart as well as reference Fe_2O_3. (d) Normalized Mn K-edge XANES spectra of pristine STMFC0.1 and reduced counterpart as well as reference Mn_2O_3.

(Fig. S3b) do not show apparent changes with the increasing Cr content. The Ti 2p peaks of STMFCx (Fig. S3c) with varying Cr contents also show negligible changes and remain +4 oxidation state. The Mn 2p spectra of STCMFx (Fig. S3d) are deconvoluted into four distinct peaks at around 641.35, 642.70, 652.95, and 654.90 eV, corresponding to Mn^{3+} $2p_{3/2}$, Mn^{4+} $2p_{3/2}$, Mn^{3+} $2p_{1/2}$, and Mn^{4+} $2p_{1/2}$, respectively [56,57]. The Mn 2p peaks of STMFCx shift to the lower binding energy with the increasing Cr content, suggesting the decreased Mn oxidation state [58, 59]. The Mn^{3+}/Mn^{4+} peak area ratio grows with the increase of Cr content. Similarly, the Fe 2p peaks of STMFCx (Fig. S3e) also shift to the lower binding energy with the increasing Cr content. This is attributed to an increase in electron density due to the lower electronegativity of Cr^{3+} compared to Fe^{3+}. The characteristic peaks of Fe^{3+} $2p_{3/2}$ and Fe^{3+} $2p_{1/2}$ are at ~708 eV and ~722 eV, respectively [60,61]. Additional shoulder peaks at slightly higher binding energies of 710.3 and 724.9 eV are assigned to Fe^{4+} $2p_{3/2}$ and $2p_{1/2}$ states, respectively. The Cr 2p spectra

of STMFC0.1 and STMFC0.2 (Fig. S3f) are deconvoluted into four distinct peaks at around ~578, ~579, ~587, and ~588 eV, corresponding to Cr(III) $2p_{3/2}$, Cr(VI) $2p_{3/2}$, Cr(III) $2p_{1/2}$, and Cr(VI) $2p_{1/2}$, respectively [62]. STMFC0.2 shows a higher peak intensity of Cr(VI) than STMFC0.1. The O1s spectra of STMFCx (Fig. S3g) show two majors peaks of lattice oxygen at 527 eV and surface adsorbed oxygen at 530.4 eV [63,64]. The increasing Cr content in the B-site leads to more high-valence Cr(VI), which is accompanied by the reduced valence of Fe and Mn. The large redox swing capability of Cr ($Cr^{3+} \leftrightarrow Cr^{6+}$) may facilitate the formation of oxygen vacancies (i.e. $\Delta\delta$) and thus enhance the H_2 production.

3.4. Solar thermochemical water splitting

3.4.1. Effect of Cr content

The STCH production of STMFCx with different Cr contents (x = 0, 0.05, 0.1, 0.15, 0.2, and 0.25) during four consecutive cycles was investigated under the same conditions (Fig. 5a). Generally, the Cr doping significantly enhances the H_2 production. The H_2 production obviously increases with the Cr content from 0 to 0.15. In the third cycle,

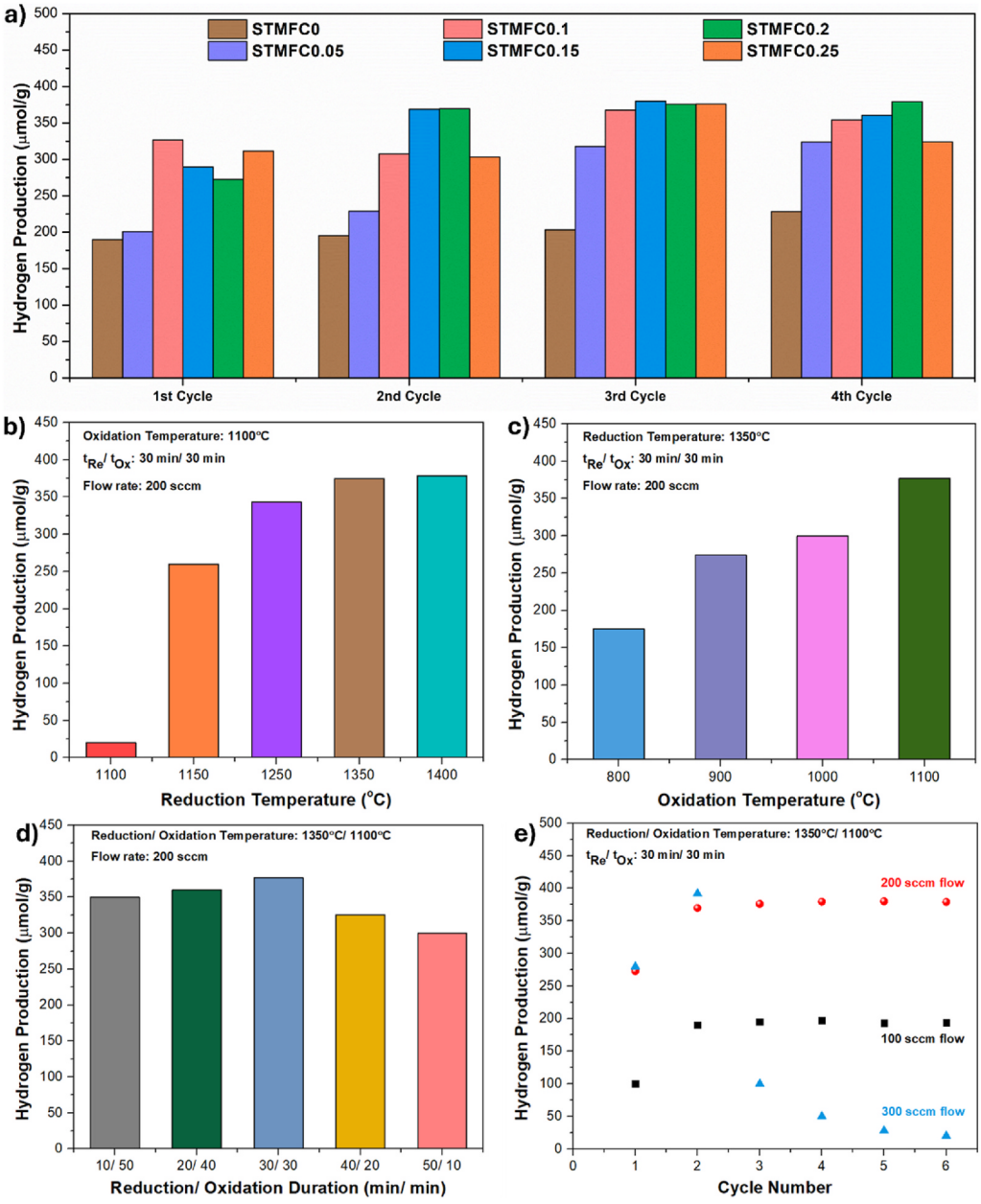

Fig. 5. a) H_2 production of $Sr(Ti_{(1-x)/3}Mn_{(1-x)/3}Fe_{(1-x)/3}Cr_x)O_3$ (x = 0, 0.05, 0.1, 0.15, 0.2, and 0.25) (STMFCx) samples for 4 consecutive STCH cycles. The reduction was conducted at 1350 °C (T_{Re}) in N_2 for 30 min and oxidation was performed at 1100 °C (T_{Ox}) in 40 vol % H_2O balanced by N_2 for 30 min with a gas flow rate of 200 sccm. b) Effect of the reduction temperature on the highest STCH production for STMFC0.2. The reduction was conducted at various T_{Re} temperatures ranging from 1100 to 1400 °C in N_2 for 30 min and oxidation was performed at 1100 °C in 40 vol % H_2O balanced by N_2 for 30 min with a gas flow rate of 200 sccm. c) Effect of the oxidation temperature on the highest STCH production for STMFC0.2. The reduction was conducted at 1350 °C in N_2 for 30 min. The oxidation was conducted at various T_{Ox} temperatures ranging from 800 to 1100 °C in 40 vol % H_2O balanced by N_2 for 30 min with a gas flow rate of 200 sccm. d) Effect of different reduction (t_{Re}) and oxidation (t_{Ox}) durations on the highest STCH production for STMFC0.2. The reduction was conducted at 1350 °C in N_2 and oxidation was performed at 1100 °C in 40 vol % H_2O balanced by N_2 with a gas flow rate of 200 sccm. The total reduction and oxidation duration for one cycle was fixed for 1 h. e) H_2 production stability of STMFC0.2 in six STCH cycles under different flow rates. The reduction was conducted at 1350 °C in N_2 for 30 min and oxidation was performed at 1100 °C in 40 vol % H_2O balanced by N_2 for 30 min.

STMFC0.15, STMFC0.2, and STMFC0.25 exhibit similar H_2 production. However, both STMFC0.15 and STMFC0.25 show degradation in H_2 production in the fourth cycle, while STMFC0.2 presents steady H_2 production increase, reaching the highest value of 380 μmol/g. This trend agrees well with the change in Δδ from the above-mentioned TPR results. Therefore, the optimal STMFC0.2 sample was primarily used to further investigate the effects of reduction and oxidation temperatures, durations and flow rates on its H_2 production.

Δδ is a major property to determine the extent of thermal reduction and H_2 production. Therefore, the correlation between Cr content and H_2 production was validated by thermochemical water splitting cycling:

$$\text{Thermal reduction step}: ABO_3 \rightarrow ABO_{3-\delta} + \frac{\delta}{2}O_2 \quad \text{(Eq. 4)}$$

$$\text{Water splitting (oxidation) step}: ABO_{3-\delta} + \delta H_2O \rightarrow ABO_3 + \delta H_2 \quad \text{(Eq. 5)}$$

From the equations of Eq. (4) and Eq. (5), the oxygen non-stoichiometry (Δδ) is directly correlated with the released O_2 amount and H_2 production. In the thermal reduction step, the formation of oxygen vacancies is accompanied by the reduction of B-site metal(s). In the following oxidation step (water splitting), the oxygen atoms from water splitting diffuse into the oxygen vacancies, which is accompanied by the oxidation of B-site metal(s). The extent of redox valence swing of B-site metal(s) plays a key role in Δδ and H_2 production. The synchrotron XAS spectra (Fig. 4b–d) demonstrate that Cr is the primary redox active metal among various B-site metal elements. Fe may show minor redox change during the high-temperature reduction. Mn and Ti might play a coordination role in stabilizing the structure. Note that the perovskite structure may collapse and decompose during the thermal reduction (formation of oxygen vacancies) without stabilizing metals in B-site.

3.4.2. Effect of reduction and oxidation temperatures

The oxidation temperature was fixed at 1100 °C. Fig. 5b displays the highest H_2 production of STMFC0.2 at different reduction temperatures. As the reduction temperature rises from 1100 to 1350 °C, the H_2 production steadily increases from 25 to 380 μmol/g. With the further increase of reduction temperature to 1400 °C, the H_2 production slightly grows to 385 μmol/g. The thermal reduction reaction of perovskite oxides is endothermic and thus a higher temperature facilitates the reduction and formation of oxygen vacancies. The reduction temperature of 1400 °C is a common lowest reduction temperature for the benchmark ceria material for STCH. At 1400 °C, ceria shows a small Δδ of 0.03 suggesting a theoretically maximum STCH production of 160 μmol/g [65–67]. At a reduction temperature lower than 1400 °C, ceria shows a negligible Δδ. As a result, most of studies on the STCH of ceria investigated the reduction temperature higher than 1400 °C. However, thermal reduction is preferably performed at temperatures lower than 1400 °C in the practical applications to minimize solar re-radiation losses and ensure the longevity of auxiliary reactor components without compromising fuel productivity [68]. Since there is no significant increase in H_2 production at the reduction of temperature of 1400 °C, 1350 °C is chosen as the optimal reduction temperature.

The impact of oxidation temperatures ranging from 800 to 1100 °C on STCH production is also examined (Fig. 5c). When the oxidation temperature exceeded 1200 °C, the alumina tube would generate a significant background level of H_2 due to its catalytic activity in direct water thermolysis [30,35]. The H_2 production declines with the decrease of oxidation temperature. Thermodynamically, a larger temperature swing by decreasing the oxidation temperature is supposed to favor the H_2 production, as the oxidation reaction is exothermic. The elevated oxidation temperature (1100 °C) rendered H_2 production 2.15 times higher than the lower oxidation temperature (800 °C) under the given reduction and oxidation duration and flow rates, as the higher oxidation temperature facilitates the reaction kinetics. Therefore, the oxidative water splitting step benefits from the increase in oxidation temperature, indicating this step is primarily limited by reaction kinetics. This has been validated by previous reports [28,35,68]. Previous reports suggest that the reoxidation temperature should be at least 200 °C lower than the thermal reduction temperature to enhance the overall H_2O splitting performance of the redox oxide [69,70]. Furthermore, a large temperature swing requires extracting a large amount of sensible heat after the reduction step and then injecting a similar amount to raise the temperature of the material in preparation for the next reduction step, requiring complex thermal management. Therefore, the reduction and oxidation temperatures were controlled at 1350 and 1100 °C, respectively.

3.4.3. Effects of the reduction and oxidation durations

This work controlled the total duration of each cycle in 1 h. STCH tests were conducted across a range of reduction/oxidation durations (in minutes) including 10/50, 20/40, 30/30, 40/20, and 50/10. Fig. 5d illustrates the H_2 production of STMFC0.2 under varying reduction and oxidation durations. The extended oxidation temperature favors the H_2 production suggesting that the oxidative water splitting step is more kinetically limited than the thermal reduction step. The highest H_2 production of 380 μmol/g was achieved under the 30-min reduction and 30-min oxidation condition. This combination may reach a tradeoff between reduction and oxidation kinetics. A shorter reduction duration results in lower H_2 production, likely due to the insufficient time for thermochemical reduction of STMFC0.2. On the other hand, shorter oxidation durations significantly decrease the H_2 production, due to the more sluggish oxidative water splitting reaction step. Therefore, the combination of 30-min reduction and 30-min oxidation may achieve a balance between sufficient reduction extent for oxygen vacancy formation during reduction step and efficient water splitting reaction during oxidation.

3.4.4. Effect of flow rates

The influence of H_2O–N_2 mixture gas flow rate in the oxidation step on the STCH production of STMFC0.2 is shown in Fig. 5e. Increasing the flow rate from 100 to 200 sccm enhanced H_2 production, as a higher flow rate for H_2O feeding can improve steam-solid interaction and mass transfer. However, further increasing the flow rate to 300 sccm leads to the significant drop of H_2 production from the third cycle. For this proof-of-concept research, an excess of steam feeding and a small quantity of perovskite oxide powder (~0.1 g) were used to ensure sufficient steam/solid contact and mass transfer for measurement of the thermodynamic limit of H_2 production. Under the large flow rate of 300 sccm, a few powders were continuously blown into the downstream water condenser, causing the powder loss from the thermal reactor center. In contrast, STMFC0.2 exhibits stable H_2 production of 380 μmol/g for 6 cycles at 200 sccm flow rate.

3.4.5. Thermochemical seawater splitting

As the STCH technology intrinsically splits water vapor into H_2 and O_2 in a chemical looping way, it is expected to flexibly function for splitting low-grade water without the reliance on the costly deionized (DI) water [71,72]. Therefore, the STCH production of STMFCx was investigated under seawater vapor feeding. Fig. 6a illustrates the H_2 production of STMFCx during 4 consecutive redox cycles. H_2 production grows with the increase of Cr content and STMFC0.2 achieves the highest hydrogen production, similar to the STCH trend when using DI water vapor feeding. Note that the seawater is pre-evaporated, and the resulting steam is intrinsically same as that from DI water. This STCH technology based on the thermochemical seawater splitting can take advantage of the low cost and abundance of seawater, especially for rural areas with limited access to purified water. Previous studies of solid oxide electrolysis cells with steam feeding from heated seawater generators have demonstrated that steam derived from seawater did not contain any contaminants and salts in the vapor form and hence the electrolysis performance remained similar [73–76]. Therefore, this

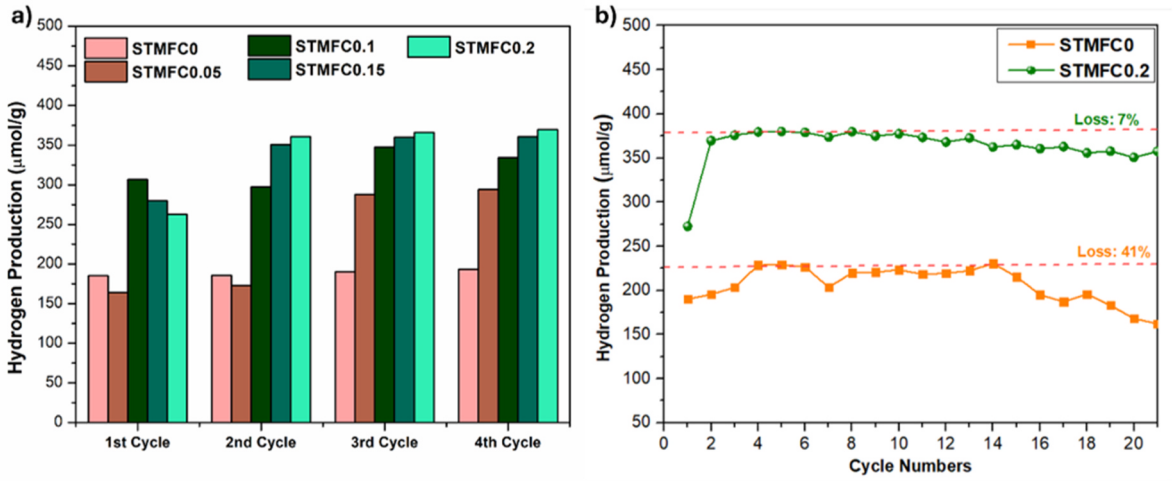

Fig. 6. a) H_2 production of STMFCx samples for 4 consecutive thermochemical seawater splitting cycles. The reduction was conducted at 1350 °C in N_2 for 30 min and oxidation was performed at 1100 °C in 40 vol % H_2O (from seawater evaporator) balanced by N_2 for 30 min with a gas flow rate of 200 sccm. b) Cycling stability of STCH production of STMFC0 and STMFC0.2. The reduction was conducted at 1350 °C in N_2 for 30 min and oxidation was performed at 1100 °C in 40 vol % DI water vapor balanced by N_2 for 30 min with a gas flow rate of 200 sccm.

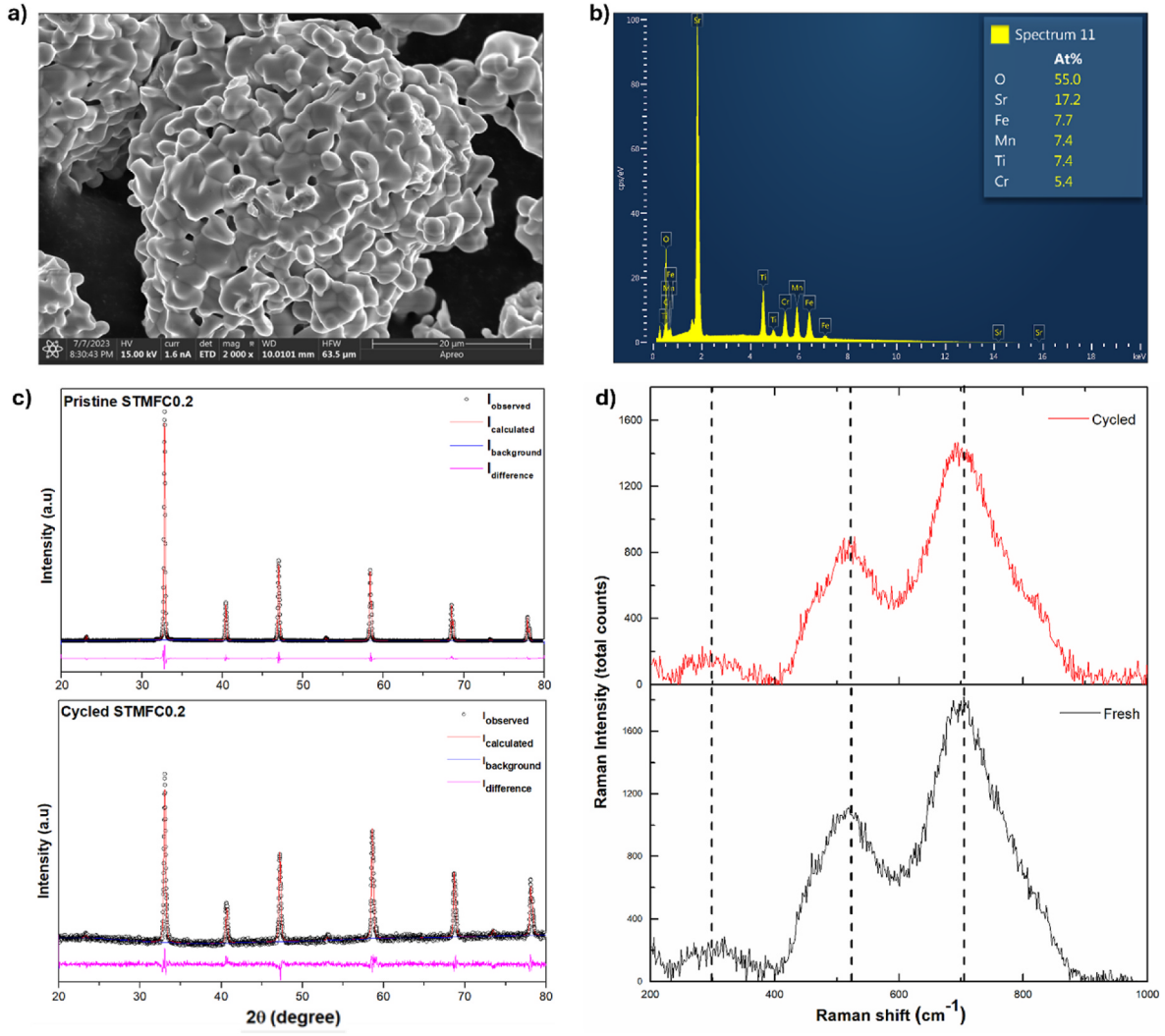

Fig. 7. a) SEM image and b) EDX spectrum of STMFC0.2 after 21 STCH cycles. c) XRD patterns and d) Raman spectra of pristine and cycled STMFC0.2.

STCH technology utilizing redox oxides composed of low-cost alkaline earth and transition metal elements is a promising technological complement to proton exchange membrane and anion exchange membrane water electrolysis that need to use deionized water and precious or critical metals [26,30,77].

3.4.6. STCH cycling stability

The STCH cycling stability of STMFC0 and STMFC0.2 was investigated under the same conditions (Fig. 6b). STMFC0 exhibits significant degradation for 21 cycles with 41 % H_2 production loss. In contrast, STMFC0.2 demonstrates good STCH stability and remains STCH production above 350 μmol/g for 21 cycles with minor H_2 production loss by 7 %.

The post-mortem characterizations were performed for cycled STMFC0.2. As shown in the SEM image (Fig. 7a), STMFC0.2 after 21 STCH cycles shows slight sintering and particle coalescence but has no segregation of secondary particles. The particle size distribution of STMFC0.2 before and after STCH cycles was analyzed from the SEM images (Fig. S2). A slight increase in the unit particle size from 2.03 ± 0.13 μm to 3.01 ± 0.01 μm was observed after cycling at alternating temperatures between 1350 and 1100 °C. Furthermore, the agglomeration of those unit particles is aggravated. These results suggest the reduced surface area of STMFC0.2 particles exposed to steam, resulting in the slightly decreased STCH production after cycles. The EDX spectrum (Fig. 7b) demonstrates that the atomic ratio of Sr, Ti, Mn, Fe, and Cr of cycled STMFC0.2 is close to that of the pristine STMFC0.2 (Fig. 3b). Furthermore, the ICP-MS results of cycled STMFC0.2 confirm its composition as $Sr(Ti_{0.262}Mn_{0.267}Fe_{0.275}Cr_{0.196})O_3$ in good agreement with the pristine nominal composition. The Rietveld Refinement of the XRD pattern confirms that cycled STMFC0.2 remains cubic perovskite crystal structure with space group $Pm\bar{3}m$ (221) and negligible change of lattice parameter (Fig. 7c and Table 4).

The Raman spectra of pristine and cycled STMFC0.2 samples show three broad peaks in the region between 200 and 700 cm^{-1} (Table 5). The characteristic Raman peaks of cycled STMFC0.2 remain largely unchanged (Fig. 7d). However, the observed weakening of Raman peak intensity and red shift of these peaks indicate structural defects within cycled STMFC0.2. All the bands in the spectra become more pronounced, indicating improved crystallization and particle growth due to sintering [78,79]. In particular, the band of fresh STMFC0.2 located around 700 cm^{-1} shifts to around 690 cm^{-1} after cycling. This can be explained by the internal strain within the samples induced by the high-temperature STCH cycles [80,81]. This indicates an increase in oxygen vacancies during cycling, resulting in weakened bond strengths and reduction in vibrational frequences [82].

The HRTEM images with EDX mapping results for STMFC0.2 before and after 21 STCH cycles were investigated. Fig. S4 shows the HRTEM image of fresh STMFC0.2. The lattice fringes with spacing of 0.279 and 0.169 nm correspond to (110) and (211) planes of the cubic perovskite structure, respectively [83]. Fig. S5 presents the HAADF-STEM EDX mapping of pristine STMFC0.2, showing the homogeneous distribution of various elements without segregation. Fig. S6 shows the HRTEM image of STMFC0.2 after 21 STCH cycles, which maintains the cubic perovskite structure with (110) and (211) planes. The HAADF-STEM EDX mapping (Fig. S7) confirms that STMFC0.2 retained the homogeneous distribution of compositional elements without obvious segregation after 21 redox cycles.

Table 4
Lattice parameters in pristine and cycled STMFC0.2 obtained from Rietveld Refinement of XRD patterns.

Sample	Lattice Parameter a (Å)	R_w (%)
Pristine - STMFC0.2	3.88053	5.51
Cycled - STMFC0.2	3.88026	4.70

Table 5
Summary of the Raman spectra peaks of pristine and cycled STMFC0.2.

Sample	Peak 1 (cm^{-1})	Peak 2 (cm^{-1})	Peak 3 (cm^{-1})
Pristine STMFC0.2	298	502	702
Cycled STMFC0.2	280	508	700

The XPS spectra of STMFC0.2 after 21 STCH cycles are compared with those of pristine counterpart (Fig. S8). The Sr 3d peaks show negligible changes, indicating no apparent surface Sr segregation. Among B-site elements, Ti 2p and Mn 2p do not show obvious changes. More Cr(VI) species are present in the cycled STMFC0.2, suggesting that Cr is likely the major redox active metal and remains oxidized in the oxidizing steam environment. The increase of Cr(VI) species in the cycled STMFC0.2 is accompanied by the slight decrease of Fe(IV). This is consistent with the XAS results. The XPS results demonstrate the redox stability of STMFC0.2 for STCH cycling. STMFC0.25 with more Cr content shows marginally higher Δδ but a minor irreversibility of oxygen non-stoichiometry (Fig. 4a). Similarly, STMFC0.25 starts to show degradation in H_2 production in the fourth cycle (Fig. 5a). This may be related to the inferior structural stabilization effect of excessive low-valence Mn and Fe (induced by doping too much high-valence Cr) in B-site (Fig. S3d and e). It has been reported that the oxygen vacancy formation energy and metal-O bond properties determined by the B-site metals influence the Δδ and STCH production in other perovskite oxide systems [36,84,85]. Future work will focus on calculating the oxygen vacancy formation energy and metal-O bond stretching for STMFCx to reveal how Cr content influences these properties.

Table 6 summarizes the STCH production of several typical perovskite oxides in comparison with that of STMFC0.2 in terms of the hydrogen production rates (H_2 production per cycle divided by the total reduction and oxidation time per cycle). Here, STMFC0.2 demonstrates a high STCH production within 1-h redox cycle. Under the similar steam concentration during the oxidation step, STMFC0.2 shows higher H_2 production than $Sr(Ti_{0.5}Mn_{0.5})O_3$, although $Sr(Ti_{0.5}Mn_{0.5})O_3$ underwent longer water splitting time in the oxidation step.

4. Conclusions

In summary, a novel family of CCPO materials, STMFCx, with tunable Cr contents from 0 to 0.25 is comprehensively investigated as redox oxides for two-step thermochemical water splitting. The developed CCPO materials only contain low-cost alkaline earth metal Sr and earth-abundant transition metals Mn, Ti, Fe and Cr, which eliminates the use of expensive rare earth and critical transition metals for STCH application. The reversible extent of reduction (Δδ) increases with the increasing Cr content. Synchrotron XAS suggests that Cr might be the major redox active element. The optimal redox oxide, STMFC0.2, demonstrates the highest H_2 production of 380 μmol/g within a short 1-h duration under optimized STCH reaction conditions and excellent H_2 production and phase stability over 21 cycles. This work also highlights the potential for extending the STCH technology to thermochemical seawater splitting. This study provides guidance in designing critical and rare earth metal-free perovskite oxides through exploring the compositionally complex ceramics for thermochemical applications such as chemical looping and heterogeneous catalysis.

Table 6
Comparison of STCH production of STMFC0.2 with that of other reported perovskite oxides.

Material	T_{Re}/T_{ox} (°C)	t_{Re}/t_{Ox} (min)	Reduction/oxidation atmosphere	H_2 production (μmol/g)	H_2 production rate (μmol/g/min)	Ref.
STMFC0.2	1350/1100	30/30	N_2/40 % H_2O with N_2	380	6.33	This work
CeO_2	1350/850	5/20	Ar/40 % H_2O with Ar	50	2	[86]
$Sr_{0.75}Ce_{0.25}MnO_3$	1350/850	5.5/20	Ar/40 % H_2O with Ar	98.0	3.84	[87]
$BaCe_{0.25}Mn_{0.75}O_3$	1350/1000	5.5/20	Ar/40 % H_2O with Ar	97.0	3.80	[86]
$Sr_{0.4}La_{0.6}Mn_{0.6}Al_{0.4}O_3$	1350/1000	30/30	He/40 % H_2O with He	307	5.12	[27]
$SrTi_{0.5}Mn_{0.5}O_3$	1350/1100	30/60	Ar/40 % H_2O with Ar	366	4.07	[68]
$CaTi_{0.5}Mn_{0.5}O_3$	1350/1100	30/60	Ar/40 % H_2O with Ar	295.1	3.28	[28]
$La_{0.7}Sr_{0.3}Mn_{0.9}Cr_{0.1}O_3$	1350/1200	1/60	N_2/84 % H_2O with N_2	160.9	2.64	[88]

Nomenclatures and Abbreviations

Nomenclatures and Acronyms	Full name
P_{O_2}	oxygen partial pressure
δ	off-stoichiometry of oxygen
Δδ	extent of reduction
Δm	mass loss
M_s	molar mass of the sample
m_s	initial sample mass
M_O	molar mass of oxygen atom
R_w	final goodness-of-fit in refinements
T_{Re}	temperature of reduction reaction
T_{Ox}	temperature of oxidation reaction
sccm	standard cubic centimeters per minute
SLMA	$Sr_xLa_{1-x}Mn_yAl_{1-y}O_{3-\delta}$
LCMA	$La_{0.6}Ca_{0.4}Mn_{1-y}Al_yO_{3-\delta}$
STMFCx	$Sr(Ti_{(1-x)/3}Mn_{(1-x)/3}Fe_{(1-x)/3}Cr_x)O$
STCH	solar thermochemical hydrogen
CCPOs	compositionally complex perovskite oxides
HEOs	high-entropy oxides
HEBM	high-energy ball mill
XRD	X-ray diffraction
CIF	crystallographic information file
ICSD	Inorganic Crystal Structure Database
ICP-MS	inductively coupled plasma mass spectrometry
XPS	X-ray photoelectron spectroscopy
SEM	scanning electron microscopy
EDX	energy-dispersive X-ray
HAADF	high angle annular dark field
STEM	scanning transmission electron microscopy
HRTEM	high-resolution transmission electron microscopy
XAS	X-ray absorption spectroscopy
TPR	temperature-programmed reduction
UHP	ultrahigh-purity
GC	gas chromatography
TCD	thermal conductivity detector
XANES	X-ray Absorption Near Edge Spectroscopy
MFC	mass flow controller

CRediT authorship contribution statement

Ha Ngoc Ngan Tran: Writing – original draft, Methodology, Investigation. **Cijie Liu:** Methodology, Investigation. **Dawei Zhang:** Methodology, Investigation. **Qingyuan Li:** Investigation. **Jingjing Yang:** Investigation. **Shaoshuai Chen:** Investigation. **Wei Li:** Writing – review & editing, Project administration, Methodology, Investigation. **Li Li:** Investigation. **Qingsong Wang:** Investigation. **Héctor A. De Santiago:** Resources, Methodology. **Liang Ma:** Resources, Methodology. **Yi Wang:** Resources, Methodology. **Gregory Collins:** Resources, Methodology. **Jian Luo:** Writing – review & editing, Supervision, Project administration, Funding acquisition. **Xingbo Liu:** Writing – review & editing, Supervision, Project administration, Funding acquisition.

Declaration of competing interest

The authors declare that they have no known competing financial interests or personal relationships that could have appeared to influence the work reported in this paper.

Acknowledgements

This work is partially supported by the U.S. Department of Energy (DOE), Office of Energy Efficiency and Renewable Energy (EERE), under the Agreement Number DE-EE0008839, managed by the Hydrogen and Fuel Cell Technologies Office in the Fiscal Year 2019H2@SCALE program. The use of the WVU Shared Research Facilities is acknowledged. The UCSD team also thanks the partial support by the National Science Foundation (NSF) under Grant Nos. DMR-2011967 and CBET-2328044, after the completion of the EERE project in July 2023, and the use of shared facilities at the San Diego Nanotechnology Infrastructure (SDNI), a member of the National Nanotechnology Coordinated Infrastructure, which is supported by the NSF grant no. ECCS-2025752. XAS experiments were carried out at BESSY II light source KMC2 beam-line and beamtime was allocated for proposal 232-12391-ST.

Appendix A. Supplementary data

Supplementary data to this article can be found online at https://doi.org/10.1016/j.ijhydene.2025.151577.

References

[1] Steinfeld A, Palumbo R. Solar thermochemical process technology. In: Encyclopedia of physical science and technology, vol. 15. Elsevier; 2003. p. 237–56. https://doi.org/10.1016/B0-12-227410-5/00698-0.
[2] Warren KJ, Tran JT, Weimer AW. A thermochemical study of iron aluminate-based materials: a preferred class for isothermal water splitting. Energy Environ Sci 2022; 15:806–21. https://doi.org/10.1039/D1EE02679H.
[3] PhanVan L, Hieu Hoang L, Nguyen Duc T. A comprehensive review of direct coupled photovoltaic-electrolyser system: sizing techniques, operating strategies, research progress, current challenges, and future recommendations. Int J Hydrog Energy 2023;48:25231–49. https://doi.org/10.1016/j.ijhydene.2023.03.257.
[4] Liu Z, Xie J, Song C, Yang X, Kalogirou SA. A review of hydrogen production through solar energy with various energy storage devices. Int J Hydrog Energy 2025. https://doi.org/10.1016/j.ijhydene.2025.01.274. S0360319925003088.
[5] El Ouardi M, El Idrissi A, Arab M, Zbair M, Haspel H, Saadi M, et al. Review of photoelectrochemical water splitting: from quantitative approaches to effect of sacrificial agents, oxygen vacancies, thermal and magnetic field on (photo) electrolysis. Int J Hydrog Energy 2024;51:1044–67. https://doi.org/10.1016/j.ijhydene.2023.09.111.
[6] Cheng W-H, De La Calle A, Atwater HA, Stechel EB, Xiang C. Hydrogen from sunlight and water: a side-by-side comparison between photoelectrochemical and solar thermochemical water-splitting. ACS Energy Lett 2021;6:3096–113. https://doi.org/10.1021/acsenergylett.1c00758.
[7] Baykara S. Experimental solar water thermolysis. Int J Hydrog Energy 2004;29: 1459–69. https://doi.org/10.1016/j.ijhydene.2004.02.011.
[8] Liu C, Park J, De Santiago HA, Xu B, Li W, Zhang D, et al. Perovskite oxide materials for solar thermochemical hydrogen production from water splitting through chemical looping. ACS Catal 2024;14:14974–5013. https://doi.org/10.1021/acscatal.4c03357.
[9] Carrillo RJ, Scheffe JR. Advances and trends in redox materials for solar thermochemical fuel production. Sol Energy 2017;156:3–20. https://doi.org/10.1016/j.solener.2017.05.032.
[10] Bayon A, De La Calle A, Stechel EB, Muhich C. Operational limits of redox metal oxides performing thermochemical water splitting. Energy Technol 2022;10: 2100222. https://doi.org/10.1002/ente.202100222.
[11] Chueh WC, Haile SM. A thermochemical study of ceria: exploiting an old material for new modes of energy conversion and CO_2 mitigation. Phil Trans R Soc A 2010; 368:3269–94. https://doi.org/10.1098/rsta.2010.0114.
[12] Bhosale RR, Takalkar G, Sutar P, Kumar A, AlMomani F, Khraisheh M. A decade of ceria based solar thermochemical H_2O/CO_2 splitting cycle. Int J Hydrog Energy 2019;44:34–60. https://doi.org/10.1016/j.ijhydene.2018.04.080.

[13] Marxer D, Furler P, Scheffe J, Geerlings H, Falter C, Batteiger V, et al. Demonstration of the entire production chain to renewable Kerosene via solar thermochemical splitting of H_2O and CO_2. Energy Fuels 2015;29:3241–50. https://doi.org/10.1021/acs.energyfuels.5b00351.

[14] Chueh WC, Falter C, Abbott M, Scipio D, Furler P, Haile SM, et al. High-Flux solar-driven thermochemical dissociation of CO_2 and H_2O using nonstoichiometric Ceria. Science 2010;330:1797–801. https://doi.org/10.1126/science.1197834.

[15] Mostafa MF, Ata-Allah SS, Refai HS. Synthesis, structure and electric studies for $La_{0.7}A_{0.3}Mn_{0.96}(In_xAl_{(1-x)})_{0.04}O_3$; a=ca and Sr perovskites. J Solid State Chem 2008;181:1056–69. https://doi.org/10.1016/j.jssc.2008.01.038.

[16] Takacs M, Hoes M, Caduff M, Cooper T, Scheffe JR, Steinfeld A. Oxygen nonstoichiometry, defect equilibria, and thermodynamic characterization of $LaMnO_3$ perovskites with Ca/Sr A-site and Al B-site doping. Acta Mater 2016;103:700–10. https://doi.org/10.1016/j.actamat.2015.10.026.

[17] Muhich CL, Ehrhart BD, Witte VA, Miller SL, Coker EN, Musgrave CB, et al. Predicting the solar thermochemical water splitting ability and reaction mechanism of metal oxides: a case study of the hercynite family of water splitting cycles. Energy Environ Sci 2015;8:3687–99. https://doi.org/10.1039/C5EE01979F.

[18] Muhich C, Steinfeld A. Principles of doping ceria for the solar thermochemical redox splitting of H_2O and CO_2. J Mater Chem A 2017;5:15578–90. https://doi.org/10.1039/C7TA04000H.

[19] Siegel NP, Miller JE, Ermanoski I, Diver RB, Stechel EB. Factors affecting the efficiency of solar driven metal oxide thermochemical cycles. Ind Eng Chem Res 2013;52:3276–86. https://doi.org/10.1021/ie400193q.

[20] Ermanoski I, Miller JE, Allendorf MD. Efficiency maximization in solar-thermochemical fuel production: challenging the concept of isothermal water splitting. Phys Chem Chem Phys 2014;16:8418–27. https://doi.org/10.1039/C4CP00978A.

[21] Emery AA, Saal JE, Kirklin S, Hegde VI, Wolverton C. High-Throughput computational screening of perovskites for thermochemical water splitting applications. Chem Mater 2016;28:5621–34. https://doi.org/10.1021/acs.chemmater.6b01182.

[22] Emery AA, Wolverton C. High-throughput DFT calculations of formation energy, stability and oxygen vacancy formation energy of ABO_3 perovskites. Sci Data 2017;4:170153. https://doi.org/10.1038/sdata.2017.153.

[23] Chen C, Yu Y, Li W, Cao C, Li P, Dou Z, et al. Mesoporous $Ce_{1-x}Zr_xO_2$ solid solution nanofibers as high efficiency catalysts for the catalytic combustion of VOCs. J Mater Chem 2011;21:12836. https://doi.org/10.1039/c1jm11685a.

[24] Li Z, Guan B, Xia F, Nie J, Li W, Ma L, et al. High-Entropy perovskite as a high-performing chromium-tolerant cathode for solid oxide fuel cells. ACS Appl Mater Interfaces 2022;14:24363–73. https://doi.org/10.1021/acsami.2c03657.

[25] Zhang J, Zhang C, Li W, Guo Q, Gao H, You Y, et al. Nitrogen-Doped perovskite as a bifunctional cathode catalyst for rechargeable lithium–oxygen batteries. ACS Appl Mater Interfaces 2018;10:5543–50. https://doi.org/10.1021/acsami.7b17289.

[26] Li W, Gao X, Xiong D, Wei F, Song W, Xu J, et al. Hydrothermal synthesis of monolithic Co_3Se_4 nanowire electrodes for oxygen evolution and overall water splitting with high efficiency and extraordinary catalytic stability. Adv Energy Mater 2017;7:1602579. https://doi.org/10.1002/aenm.201602579.

[27] McDaniel AH, Miller EC, Arifin D, Ambrosini A, Coker EN, O'Hayre R, et al. Sr- and Mn-doped $LaAlO_{3-\delta}$ for solar thermochemical H2 and CO production. Energy Environ Sci 2013;6:2424. https://doi.org/10.1039/c3ee41372a.

[28] Qian X, He J, Mastronardo E, Baldassarri B, Yuan W, Wolverton C, et al. Outstanding properties and performance of $CaTi_{0.5}Mn_{0.5}O_{3-\delta}$ for solar-driven thermochemical hydrogen production. Matter 2021;4:688–708. https://doi.org/10.1016/j.matt.2020.11.016.

[29] Gao Y, Zhang M, Mao Y, Cao H, Zhang S, Wang W, et al. Microwave-triggered low temperature thermal reduction of Zr-modified high entropy oxides with extraordinary thermochemical H_2 production performance. Energy Conv Manag 2022;252:115125. https://doi.org/10.1016/j.enconman.2021.115125.

[30] Liu C, Zhang D, Li W, Trindell JA, King KA, Bishop SR, et al. Manganese-based A-site high-entropy perovskite oxide for solar thermochemical hydrogen production. J Mater Chem A 2024;12:3910–22. https://doi.org/10.1039/D3TA03554A.

[31] Bishop SR, Zhang D, Liu C, Li W, Salinas PA, Smith AI, et al. Oxygen non-stoichiometry and point defect equilibria in $(La_{1/6}Pr_{1/6}Nd_{1/6}Gd_{1/6}Ba_{1/6}Sr_{1/6})MnO_{3-\delta}$. ECS Trans 2023;111:1135–8. https://doi.org/10.1149/11106.1135ecst.

[32] Zhai S, Rojas J, Ahlborg N, Lim K, Toney MF, Jin H, et al. The use of poly-cation oxides to lower the temperature of two-step thermochemical water splitting. Energy Environ Sci 2018;11:2172–8. https://doi.org/10.1039/C8EE00050F.

[33] Wright AJ, Luo J. A step forward from high-entropy ceramics to compositionally complex ceramics: a new perspective. J Mater Sci 2020;55:9812–27. https://doi.org/10.1007/s10853-020-04583-w.

[34] Wright AJ, Wang Q, Huang C, Nieto A, Chen R, Luo J. From high-entropy ceramics to compositionally-complex ceramics: a case study of fluorite oxides. J Eur Ceram Soc 2020;40:2120–9. https://doi.org/10.1016/j.jeurceramsoc.2020.01.015.

[35] Zhang D, De Santiago HA, Xu B, Liu C, Trindell JA, Li W, et al. Compositionally complex perovskite oxides for solar thermochemical water splitting. Chem Mater 2023;35:1901–15. https://doi.org/10.1021/acs.chemmater.2c03054.

[36] Xu B, Park J, Zhang D, De Santiago HA, Li W, Liu X, et al. Local ordering, distortion, and redox activity in $(La_{0.75}Sr_{0.25})(Mn_{0.25}Fe_{0.25}Co_{0.25}Al_{0.25})O_3$ investigated by a computational workflow for compositionally complex Perovskite oxides. Chem Mater 2024;36:4990–5001. https://doi.org/10.1021/acs.chemmater.3c03038.

[37] Zhang D, Park J, Xu B, Liu C, Li W, Liu X, et al. Unusual aliovalent doping effects on oxygen non-stoichiometry in medium-entropy compositionally complex perovskite oxides. Dalton Trans 2023;52:1082–8. https://doi.org/10.1039/D2DT03759A.

[38] Tran HNN, Li W, Liu X. Perovskite oxide redox materials for two-step solar thermochemical CO_2 splitting. Chem Eng J 2024;500:156613. https://doi.org/10.1016/j.cej.2024.156613.

[39] Weber MC, Kreisel J, Thomas PA, Newton M, Sardar K, Walton RI. Phonon Raman scattering of $RCrO_3$ perovskites (R = Y , La, Pr, Sm, Gd, Dy, Ho, Yb, Lu). Phys Rev B 2012;85:054303. https://doi.org/10.1103/PhysRevB.85.054303.

[40] Sediva E, Rupp JLM. Raman spectra and defect chemical characteristics of $Sr(Ti,Fe)O_{3-y}$ solid solution of bulk pellets *vs.* thin films. J Mater Chem A 2023;11:26752–63. https://doi.org/10.1039/D3TA04818G.

[41] Nilsen WG, Skinner JG. Raman spectrum of strontium titanate. J Chem Phys 1968;48:2240–8. https://doi.org/10.1063/1.1669418.

[42] Martín-Carrón L, De Andrés A, Martínez-Lope MJ, Casais MT, Alonso JA. Raman phonons as a probe of disorder, fluctuations, and local structure in doped and undoped orthorhombic and rhombohedral manganites. Phys Rev B 2002;66:174303. https://doi.org/10.1103/PhysRevB.66.174303.

[43] Runka T, Berkowski M. Perovskite $La_{1-x}Sr_xGa_{1-y}Mn_yO_3$ solid solution crystals: raman spectroscopy characterization. J Mater Sci 2012;47:5393–401. https://doi.org/10.1007/s10853-012-6422-2.

[44] Todorov ND, Abrashev MV, Ivanov VG, Tsutsumanova GG, Marinova V, Wang Y-Q, et al. Comparative Raman study of isostructural $YCrO_3$ and $YMnO_3$: effects of structural distortions and twinning. Phys Rev B 2011;83:224303. https://doi.org/10.1103/PhysRevB.83.224303.

[45] Van Minh N, Phuong DTT. $SrTi_{1-x}Fe_xO_3$ nanoparticle: a study of structural, optical, impedance and magnetic properties. J Exp Nanosci 2011;6:226–37. https://doi.org/10.1080/17458080.2010.492841.

[46] Dubroka A, Humlíček J, Abrashev MV, Popović ZV, Sapiña F, Cantarero A. Raman and infrared studies of $La_{1-y}Sr_yMn_{1-x}M_xO_3$ (M = Cr, Co, Cu, Zn, Sc or Ga): oxygen disorder and local vibrational modes. Phys Rev B 2006;73:224401. https://doi.org/10.1103/PhysRevB.73.224401.

[47] Imada M, Fujimori A, Tokura Y. Metal-insulator transitions. Rev Mod Phys 1998;70:1039–263. https://doi.org/10.1103/RevModPhys.70.1039.

[48] Meijer GI, Staub U, Janousch M, Johnson SL, Delley B, Neisius T. Valence states of Cr and the insulator-to-metal transition in Cr-doped $SrTiO_3$. Phys Rev B 2005;72:155102. https://doi.org/10.1103/PhysRevB.72.155102.

[49] Kotnana G, Jammalamadaka SN. Band gap tuning and orbital mediated electron–phonon coupling in $HoFe_{1-x}Cr_xO_3$ ($0 \leq x \leq 1$). J Appl Phys 2015;118:124101. https://doi.org/10.1063/1.4931155.

[50] Sediva E, Defferriere T, Perry NH, Tuller HL, Rupp JLM. In situ method correlating raman vibrational characteristics to chemical expansion via oxygen nonstoichiometry of perovskite thin films. Adv Mater 2019;31:1902493. https://doi.org/10.1002/adma.201902493.

[51] Vračar M, Kuzmin A, Merkle R, Purans J, Kotomin EA, Maier J, et al. Jahn-Teller distortion around Fe^{4+} in $Sr(Fe_xTi_{1-x})O_{3-\delta}$ from X-ray absorption spectroscopy, X-ray diffraction, and vibrational spectroscopy. Phys Rev B 2007;76:174107. https://doi.org/10.1103/PhysRevB.76.174107.

[52] Souza Filho AG, Faria JLB, Guedes I, Sasaki JM, Freire PTC, Freire VN, et al. Evidence of magnetic polaronic states in $La_{0.70}Sr_{0.30}Mn_{1-x}Fe_xO_3$ manganites. Phys Rev B 2003;67:052405. https://doi.org/10.1103/PhysRevB.67.052405.

[53] Sanders MD, Bergeson-Keller AM, Coker EN, O'Hayre RP. A thermogravimetric temperature-programmed thermal redox protocol for rapid screening of metal oxides for solar thermochemical hydrogen production. Front Energy Res 2022;10:856943. https://doi.org/10.3389/fenrg.2022.856943.

[54] Andreasson BP, Janousch M, Staub U, Meijer GI, Delley B. Resistive switching in Cr doped $SrTiO_3$: an X-ray absorption spectroscopy study. Mater Sci Eng B 2007;144:60–3. https://doi.org/10.1016/j.mseb.2007.07.059.

[55] Sinder M, Burshtein Z, Pelleg J. Theory of oxidation/reduction-induced chromium ion valence transformations in Cr,Ca:YAG crystals. ArXiv 2007. https://doi.org/10.48550/ARXIV.0708.1798.

[56] Hastuti E, Subhan A, Amonpattaratkit P, Zainuri M, Suasmoro S. The effects of Fe-doping on MnO_2 : phase transitions, defect structures and its influence on electrical properties. RSC Adv 2021;11:7808–23. https://doi.org/10.1039/D0RA10376D.

[57] Kumar R, Bhowmik RN, Sinha AK. Role of A site doped rare earth (Gd^{3+} and Ho^{3+}) ions in the lattice structure and magnetic properties of biphasic $La_{2-x}RE_xNiMnO_6$ (RE = Gd, Ho, x = 0.1) double perovskites. J Alloy Compd 2022;920:165917. https://doi.org/10.1016/j.jallcom.2022.165917.

[58] Chen X, Li W, Xu Y, Zeng Z, Tian H, Velayutham M, et al. Charging activation and desulfurization of MnS unlock the active sites and electrochemical reactivity for Zn-ion batteries. Nano Energy 2020;75:104869. https://doi.org/10.1016/j.nanoen.2020.104869.

[59] Jain N, Roy A. Phase & morphology engineered surface reducibility of MnO_2 nano-heterostructures: implications on catalytic activity towards CO oxidation. Mater Res Bull 2020;121:110615. https://doi.org/10.1016/j.materresbull.2019.110615.

[60] Yamashita T, Hayes P. Analysis of XPS spectra of Fe^{2+} and Fe^{3+} ions in oxide materials. Appl Surf Sci 2008;254:2441–9. https://doi.org/10.1016/j.apsusc.2007.09.063.

[61] Li X, Zhang H, Liu X, Li S, Zhao M. XPS study on O(1s) and Fe(2p) for nanocrystalline composite oxide $LaFeO_3$ with the perovskite structure. Mater Chem Phys 1994;38:355–62. https://doi.org/10.1016/0254-0584(94)90213-5.

[62] Słoczyński J, Janas J, Machej T, Rynkowski J, Stoch J. Catalytic activity of chromium spinels in SCR of NO with NH_3. Appl Catal, B 2000;24:45–60. https://doi.org/10.1016/S0926-3373(99)00093-4.

[63] Li Q, Ho H-P, Zeng Z, Li W, Wang Q, Dong K, et al. Local structural distortion and energy gradient enhance lithium ionic conductivity in high-entropy oxide. Mater Today 2025. https://doi.org/10.1016/j.mattod.2025.08.012.

[64] Merino NA, Barbero BP, Eloy P, Cadús LE. $La_{1-x}Ca_xCoO_3$ perovskite-type oxides: identification of the surface oxygen species by XPS. Appl Surf Sci 2006;253:1489–93. https://doi.org/10.1016/j.apsusc.2006.02.035.
[65] Panlener RJ, Blumenthal RN, Garnier JE. A thermodynamic study of nonstoichiometric cerium dioxide. J Phys Chem Solids 1975;36:1213–22. https://doi.org/10.1016/0022-3697(75)90192-4.
[66] Perry J, De La Calle A, Jones TW, Donne SW, Coronado JM, Bayon A. Thermo-electrochemical hydrogen production based on ceria. Int J Hydrog Energy 2025;141:1172–81. https://doi.org/10.1016/j.ijhydene.2025.02.083.
[67] Le Gal A, Abanades S. Dopant incorporation in Ceria for enhanced water-splitting activity during solar thermochemical hydrogen generation. J Phys Chem C 2012;116:13516–23. https://doi.org/10.1021/jp302146c.
[68] Qian X, He J, Mastronardo E, Baldassarri B, Wolverton C, Haile SM. Favorable Redox thermodynamics of $SrTi_{0.5}Mn_{0.5}O_{3-\delta}$ in solar thermochemical water splitting. Chem Mater 2020;32:9335–46. https://doi.org/10.1021/acs.chemmater.0c03278.
[69] Lee MM, Teuscher J, Miyasaka T, Murakami TN, Snaith HJ. Efficient hybrid solar cells based on meso-superstructured organometal halide perovskites. Science 2012;338:643–7. https://doi.org/10.1126/science.1228604.
[70] Kay A, Grätzel M. Low cost photovoltaic modules based on dye sensitized nanocrystalline titanium dioxide and carbon powder. Sol Energy Mater Sol Cells 1996;44:99–117. https://doi.org/10.1016/0927-0248(96)00063-3.
[71] Yu Y, Cao C, Li W, Li P, Qu J, Song W. Low-cost synthesis of robust anatase polyhedral structures with a preponderance of exposed {001} facets for enhanced photoactivities. Nano Res 2012;5:434–42. https://doi.org/10.1007/s12274-012-0226-1.
[72] Li W, Tian H, Ma L, Wang Y, Liu X, Gao X. Low-temperature water electrolysis: fundamentals, progress, and new strategies. Mater Adv 2022;3:5598–644. https://doi.org/10.1039/D2MA00185C.
[73] Lim CK, Liu Q, Zhou J, Sun Q, Chan SH. High-temperature electrolysis of synthetic seawater using solid oxide electrolyzer cells. J Power Sources 2017;342:79–87. https://doi.org/10.1016/j.jpowsour.2016.12.019.
[74] Liu Z, Han B, Lu Z, Guan W, Li Y, Song C, et al. Efficiency and stability of hydrogen production from seawater using solid oxide electrolysis cells. Appl Energy 2021;300:117439. https://doi.org/10.1016/j.apenergy.2021.117439.
[75] Hu X, Yang Y, Han B, Huang X, Lei J, Sang J, et al. Efficiency and stability of seawater electrolysis through flat-tube solid oxide cell stack without air. Int J Hydrog Energy 2024;55:909–16. https://doi.org/10.1016/j.ijhydene.2023.11.138.
[76] Tian H, Li W, Lee Y-L, Zheng H, Li Q, Ma L, et al. Conformally coated scaffold design using water-tolerant $Pr_{1.8}Ba_{0.2}NiO_{4.1}$ for protonic ceramic electrochemical cells with 5,000-h electrolysis stability. Nat Energy 2025;10:890–903. https://doi.org/10.1038/s41560-025-01800-1.
[77] Li W, Xiong D, Gao X, Song W-G, Xia F, Liu L. Self-supported Co-Ni-P ternary nanowire electrodes for highly efficient and stable electrocatalytic hydrogen evolution in acidic solution. Catal Today 2017;287:122–9. https://doi.org/10.1016/j.cattod.2016.09.007.
[78] Jacot R, Naik JM, Moré R, Michalsky R, Steinfeld A, Patzke GR. Reactive stability of promising scalable doped ceria materials for thermochemical two-step CO_2 dissociation. J Mater Chem A 2018;6:5807–16. https://doi.org/10.1039/C7TA10966K.
[79] Lin X-M, Li L-P, Li G-S, Su W-H. Transport property and Raman spectra of nanocrystalline solid solutions $Ce_{0.8}Nd_{0.2}O_{2-\delta}$ with different particle size. Mater Chem Phys 2001;69:236–40. https://doi.org/10.1016/S0254-0584(00)00409-0.
[80] Zhao B, Huang C, Ran R, Wu X, Weng D. Two-step thermochemical looping using modified ceria-based materials for splitting CO_2. J Mater Sci 2016;51:2299–306. https://doi.org/10.1007/s10853-015-9534-7.
[81] Sellick DR, Aranda A, García T, López JM, Solsona B, Mastral AM, et al. Influence of the preparation method on the activity of ceria zirconia mixed oxides for naphthalene total oxidation. Appl Catal, B 2013;132–133:98–106. https://doi.org/10.1016/j.apcatb.2012.11.036.
[82] Yu X, Hu C, Ji P, Ren Y, Zhao H, Liu G, et al. Optically transparent ultrathin NiCo alloy oxide film: precise oxygen vacancy modulation and control for enhanced electrocatalysis of water oxidation. Appl Catal, B 2022;310:121301. https://doi.org/10.1016/j.apcatb.2022.121301.
[83] Xing G, Zhao L, Sun T, Su Y, Wang X. Hydrothermal derived nitrogen doped $SrTiO_3$ for efficient visible light driven photocatalytic reduction of chromium(VI). SpringerPlus 2016;5:1132. https://doi.org/10.1186/s40064-016-2804-2.
[84] Wexler RB, Sai Gautam G, Bell RT, Shulda S, Strange NA, Trindell JA, et al. Multiple and nonlocal cation redox in ca–ce–ti–mn oxide perovskites for solar thermochemical applications. Energy Environ Sci 2023;16:2550–60. https://doi.org/10.1039/D3EE00234A.
[85] Morelock RJ, Tran JT, Trindell JA, Bare ZJL, McDaniel AH, Weimer AW, et al. Computationally guided discovery of mixed Mn/Ni perovskites for solar thermochemical hydrogen production at high H_2 conversion. Chem Mater 2024;36:5331–42. https://doi.org/10.1021/acs.chemmater.3c02807.
[86] Barcellos D R, Sanders MD, Tong J, McDaniel AH, O'Hayre RP. $BaCe_{0.25}Mn_{0.75}O_{3-\delta}$ — a promising perovskite-type oxide for solar thermochemical hydrogen production. Energy Environ Sci 2018;11:3256–65. https://doi.org/10.1039/C8EE01989D.
[87] Scheffe JR, McDaniel AH, Allendorf MD, Weimer AW. Kinetics and mechanism of solar-thermochemical H_2 production by oxidation of a cobalt ferrite–zirconia composite. Energy Environ Sci 2013;6:963. https://doi.org/10.1039/c3ee23568h.
[88] Gokon N, Hara K, Sugiyama Y, Bellan S, Kodama T, Hyun-seok C. Thermochemical two-step water splitting cycle using perovskite oxides based on $LaSrMnO_3$ redox system for solar H_2 production. Thermochim Acta 2019;680:178374. https://doi.org/10.1016/j.tca.2019.178374.